iScience

CellPress
OPEN ACCESS

Article

Identification of IQCH as a calmodulin-associated protein required for sperm motility in humans

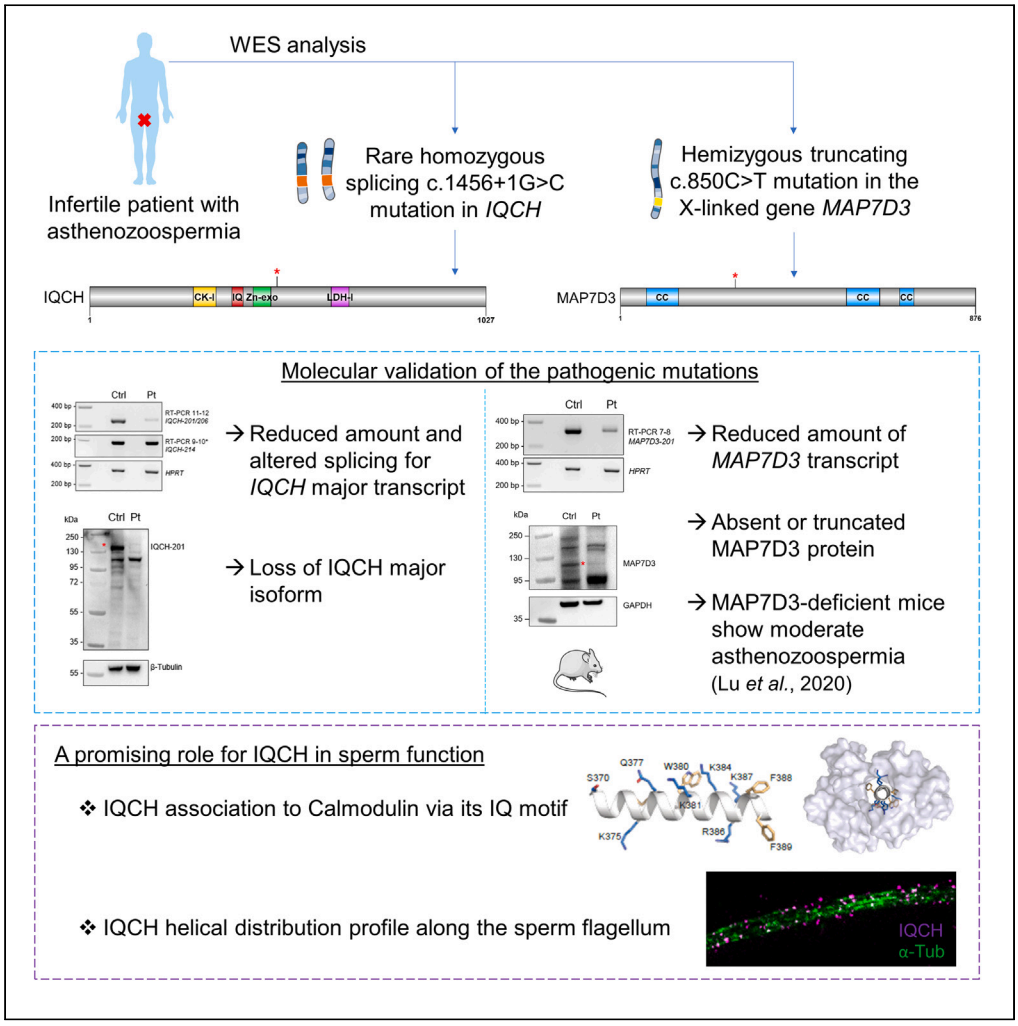

Emma Cavarocchi, Camille Sayou, Patrick Lorès, ..., Pierre F. Ray, Emmanuel Dulioust, Aminata Touré

aminata.toure@inserm.fr

Highlights

Cumulative mutations in *MAPD73* and *IQCH* identified in human asthenozoospermia

IQCH is a calmodulin-associated protein in human sperm flagellum

IQCH is required for sperm motility and capacitation in humans

Cavarocchi et al., iScience *26*, 107354
August 18, 2023
https://doi.org/10.1016/j.isci.2023.107354

iScience

CellPress
OPEN ACCESS

Article

Identification of IQCH as a calmodulin-associated protein required for sperm motility in humans

Emma Cavarocchi,[1] Camille Sayou,[1] Patrick Lorès,[2] Caroline Cazin,[1,3] Laurence Stouvenel,[2] Elma El Khouri,[2] Charles Coutton,[1,4] Zine-Eddine Kherraf,[3] Catherine Patrat,[2,5] Jérôme Govin,[1] Nicolas Thierry-Mieg,[6] Marjorie Whitfield,[1] Pierre F. Ray,[1,3] Emmanuel Dulioust,[2,5] and Aminata Touré[1,7,*]

SUMMARY

Sperm fertilization ability mainly relies on proper sperm progression through the female genital tract and capacitation, which involves phosphorylation signaling pathways triggered by calcium and bicarbonate. We performed exome sequencing of an infertile asthenozoospermic patient and identified truncating variants in *MAP7D3*, encoding a microtubule-associated protein, and *IQCH*, encoding a protein of unknown function with enzymatic and signaling features. We demonstrate the deleterious impact of both variants on sperm transcripts and proteins from the patient. We show that, *in vitro*, patient spermatozoa could not induce the phosphorylation cascades associated with capacitation. We also provide evidence for IQCH association with calmodulin, a well-established calcium-binding protein that regulates the calmodulin kinase. Notably, we describe IQCH spatial distribution around the sperm axoneme, supporting its function within flagella. Overall, our work highlights the cumulative pathological impact of gene mutations and identifies IQCH as a key protein required for sperm motility and capacitation.

INTRODUCTION

The sperm flagellum is composed of an axonemal microtubule-based skeleton in which multiprotein complexes are coordinated to regulate beating of the organelle and ultimately ensure sperm progression to reach the oocyte. In contrast to cilia and protist flagella, which share this evolutionarily conserved microtubular structure, the sperm axoneme is encircled by specific peri-axonemal structures (i.e., the fibrous and mitochondrial sheath) that ensure proper integrity and flexibility of the organelle and constitute a molecular protein hub for energy metabolism and motility signaling pathways.[1] Intuitively, a correct flagellar structure appears to be essential for efficient sperm progression. In addition, post-testicular maturation events have long been known to be compulsory for the activation of sperm motility and acquisition of fertilization potential.[2,3] Hence, although sperm cells produced in the testis are structurally differentiated, they lack progressive motility and are unable to fertilize the oocyte unless they undergo a series of maturation events that occur during their transit through the male and female genital tracts.[4–6] Sperm cells first acquire motility during transport through the intermediate segment of the epididymis, before storage in a quiescent state in the caudal region of the epididymis.[7] After ejaculation and upon exposure to the basic pH of the female genital tract, sperm cells are activated by a process called capacitation, which increases the amplitude and velocity of sperm flagellar beating (i.e., hyperactivation) and ultimately enables penetration of the sperm cell through the zona pellucida and cumulus cell layers surrounding the oocyte and its specific recognition.[8] Certain biochemical, electrophysiological, and signaling pathways that sustain the functional maturation of sperm cells have been elucidated; in particular, a complex series of ion exchange events that occur between the luminal milieus of the genital tracts and sperm cells have been shown to induce protein phosphorylation, a hallmark of capacitation.[9,10] In this context, a panoply of membrane ion channels and exchangers have been identified and mutations of a number of them have shown to be responsible for asthenozoospermia, both in mice and in humans.[11–13] Importantly, soluble adenylyl cyclase and calmodulin, directly regulated by bicarbonate and/or calcium fixation, are well-established key signaling proteins that trigger sperm protein phosphorylation cascades by modulating protein kinase A (PKA) and calmodulin-dependent protein kinase, respectively.[10] Here, we first performed genetic analysis of an infertile patient and demonstrated the pathogenicity and cumulative effects of two truncating variants identified in

[1]Institute for Advanced Biosciences, INSERM U 1209, CNRS UMR 5309, Université Grenoble Alpes, 38000 Grenoble, France

[2]Institut Cochin, INSERM U1016, CNRS UMR 8104, Université Paris Cité, 75014 Paris, France

[3]CHU de Grenoble Alpes, UM GI-DPI, 38000 Grenoble, France

[4]CHU Grenoble Alpes, UM de Génétique Chromosomique, Grenoble, France

[5]Laboratoire d'Histologie Embryologie - Biologie de la Reproduction - CECOS Groupe Hospitalier Universitaire Paris Centre, Assistance Publique-Hôpitaux de Paris, 75014 Paris, France

[6]University Grenoble Alpes, CNRS, UMR 5525, TIMC / MAGe, 38000 Grenoble, France

[7]Lead contact

*Correspondence: aminata.toure@inserm.fr

https://doi.org/10.1016/j.isci.2023.107354

MAP7D3 and *IQCH*. In addition, we combined functional sperm analysis, *in silico* protein structure modeling, and high-resolution subcellular imaging to identify IQCH as a flagellar protein associated with calmodulin, which is required for human sperm motility and capacitation. This work not only contributes to improving the genetic diagnosis of male infertility but also provides insights into the functional regulatory networks underlying the acquisition of sperm fertilization potential.

RESULTS

Exome sequencing of an infertile patient presenting with asthenozoospermia identifies truncating variants in *MAP7D3* and *IQCH*

The patient of this study originated from North Africa and consulted for primary infertility at the age of 46 at the Reproductive Biology Center of the Cochin Hospital (Paris, France). His medical chart mentioned obesity and a mild form of diabetes, hypertension, hepatitis B (diagnosed in 2009 and treated), and a varicocelectomy performed in 1997. The patient declared no consumption of alcohol, tobacco, or other gonadotoxic exposures. His wife, aged 40, was diagnosed with only one uterine horn but showed a good ovarian reserve. The couple had previously benefited from four attempts of intracytoplasmic sperm injection in a Tunisian clinic, one of which resulted in an extra-uterine pregnancy. A single attempt was performed at the Cochin Hospital; one embryo obtained, but no pregnancy was achieved after transfer. The patient originated from a consanguineous family; his parents were cousins and he was also married to his cousin (see Figure S1A for the genealogical tree). Semen analyses performed between 2012 and 2016 revealed asthenoteratozoospermia associated with normal values of sperm concentration (mean of 87.2 10^6/mL, n = 3, normal value >15 10^6/mL) and viability rate (mean of 60.6%, n = 3, normal value >58%) (Table S1). Total and progressive sperm motility were significantly reduced relative to normal values, although not completely abolished: total motility 15%–30% (normal value >40%) and progressive motility 10%–20% (normal value >32%). Although the mean percentage of spermatozoa with typical morphology was reduced, mainly due to coiled flagella (Table S1, Figure S1B), the sperm flagella did not show major assembly defects, such as short, absent, or irregular caliber flagella, a phenotype previously associated with severe asthenozoospermia and known as multiple morphological abnormalities of sperm flagella (MMAF).[14,15] Transmission electron microscopy (TEM) showed near normal axonemal organization (9 + 2), thus formally excluding a MMAF phenotype (Figure S1C). Overall, the phenotype of this patient was classified as moderate functional asthenozoospermia. Bioinformatic analyses and filtering of exome sequencing data from the patient identified several gene variants, most of which consisted of missense variants with a moderate-high predicted impact on gene function (Table S2). Only two variants were predicted to severely impact a gene's function and were thus further investigated: a hemizygous variant in the X-linked gene *MAP7D3* (*c.850C>T*) and a homozygous mutation affecting a splicing donor site of *IQCH* (*c.1456+1G>C*).

The *MAP7D3 c.850C>T* variant affects *MAP7D3* transcript and protein levels in sperm from the patient

The first identified variant consisted of a hemizygous *c.850C>T* substitution in exon 8 of the X-linked gene *MAP7D3* (MIM 300930) (Figure 1A). *MAP7D3* is located on the X chromosome and contains 19 exons, resulting in a predicted protein of 876 amino acids, with several coiled-coil domains, belonging to the family of microtubule-associated proteins (UniProtKB: Q8IWC1), which promote tubulin stability and polymerization[16] (Figure 1A). MAP7D3 was previously shown to localize to the sperm flagella in humans[16] and recent work reported that, although fertile, MAP7D3-deficient mice showed a slight decrease in sperm motility.[17] The identified *MAP7D3 c.850C>T* variant was not reported in databases (gnomAD, HGMD) and was predicted to induce a premature stop codon at position p.Gln284 of the protein. We therefore tested for a potential contribution of this variant to the asthenozoospermia phenotype. We first performed RT-PCR on a panel of human tissues to define the tissue distribution of *MAP7D3* transcript isoforms. In accordance with public database records (Illumina Body Map, The Human Protein Atlas database, ReproGenomics Viewer), we detected ubiquitous expression of the major transcript *MAP7D3-201*. The transcript isoform *MAP7D3-202*, lacking the 5′ region of exon 8, which is targeted by the *c.850C>T* variant, showed a more limited expression profile and, although detected in the testis, was absent from ejaculated spermatozoa (Figure 1B). Interestingly, single-cell RNA sequencing datasets from human adult testis (ReproGenomics viewer,[18]) showed the *MAP7D3* transcript throughout all stages of spermatogenesis, with a peak in spermatogonial stem cells, differentiating spermatogonia and Sertoli cells (Figure 1C), the expression in Sertoli cells being consistent with the reported functions of MAP proteins in the cytoskeletal dynamics of Sertoli cells during spermatogenesis.[19]

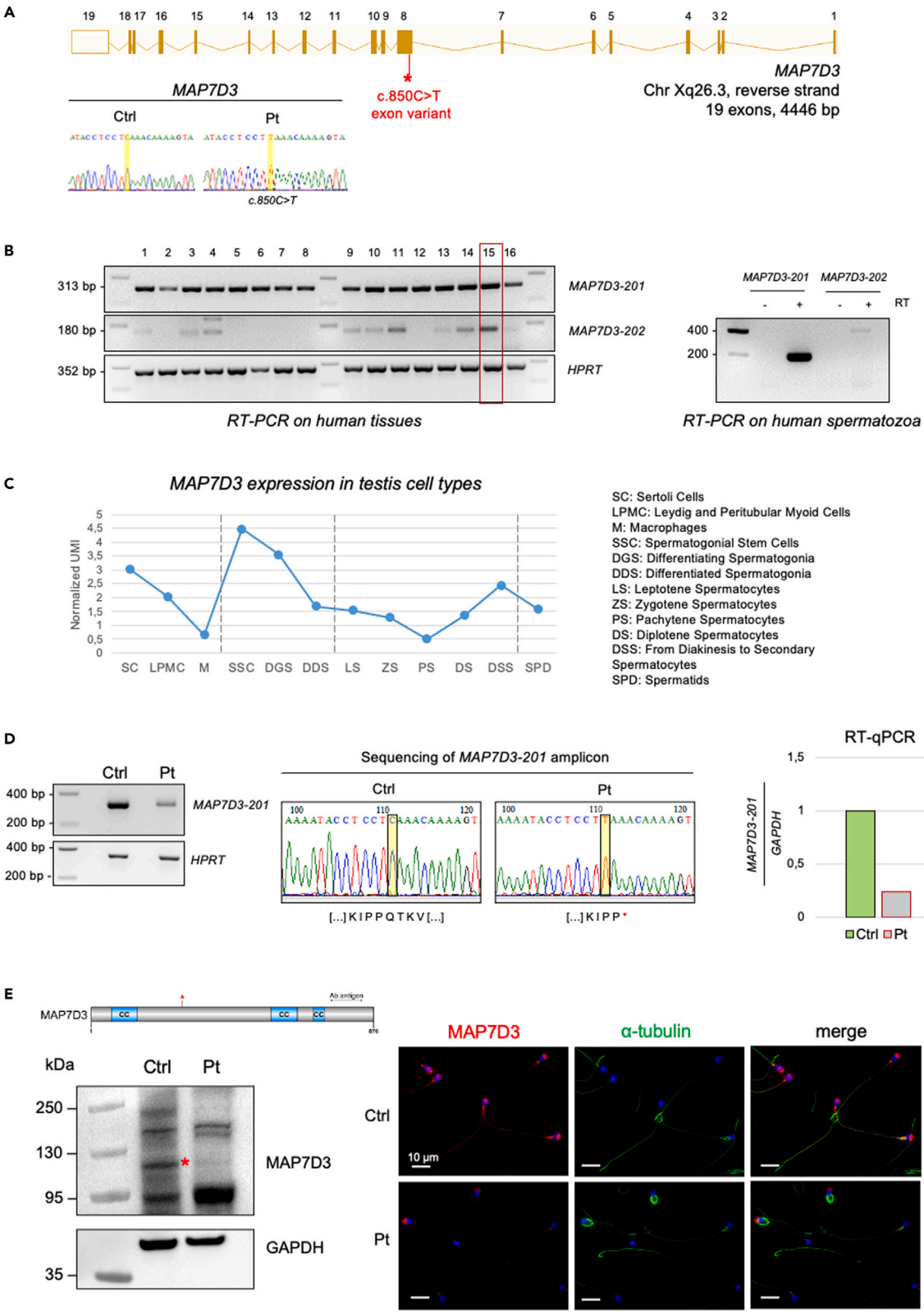
A
MAP7D3
c.850C>T
exon variant
MAP7D3
Chr Xq26.3, reverse strand
19 exons, 4446 bp
Ctrl
Pt
c.850C>T
B
313 bp
180 bp
352 bp
MAP7D3-201
MAP7D3-202
HPRT
RT-PCR on human tissues
MAP7D3-201
MAP7D3-202
RT
400
200
RT-PCR on human spermatozoa
C
MAP7D3 expression in testis cell types
Normalized UMI
SC LPMC M SSC DGS DDS LS ZS PS DS DSS SPD
SC: Sertoli Cells
LPMC: Leydig and Peritubular Myoid Cells
M: Macrophages
SSC: Spermatogonial Stem Cells
DGS: Differentiating Spermatogonia
DDS: Differentiated Spermatogonia
LS: Leptotene Spermatocytes
ZS: Zygotene Spermatocytes
PS: Pachytene Spermatocytes
DS: Diplotene Spermatocytes
DSS: From Diakinesis to Secondary Spermatocytes
SPD: Spermatids
D
Ctrl
Pt
400 bp
200 bp
MAP7D3-201
HPRT
Sequencing of MAP7D3-201 amplicon
[...]KIPPQTKV[...]
[...]KIPP*
RT-qPCR
MAP7D3-201 / GAPDH
Ctrl
Pt
E
MAP7D3
Ab antigen
kDa
250
130
95
35
MAP7D3
GAPDH
MAP7D3
α-tubulin
merge
Ctrl
Pt
10 µm

Figure 1. Characterization of the *MAP7D3* hemizygous *c.850C>T* variant identified in the patient

(A) Representation of the *MAP7D3* gene with exons (bars) and introns (connections) adapted from Ensembl genome browser. The red asterisk indicates the identified *c.850C>T* mutation, which was also confirmed by Sanger sequencing on genomic DNA from the patient (see electropherogram).

(B) RT-PCR analysis of the *MAP7D3-201* transcript isoform (exons 7–8) and *MAP7D3-202* transcript isoform (exon 7-8 junction) in a panel of human tissues and mature spermatozoa. Tissues: 1: heart, 2: brain, 3: placenta, 4: lung, 5: liver, 6: muscle, 7: kidney, 8: pancreas, 9: colon, 10: ovary, 11: leukocytes, 12: prostate, 13: intestine, 14: spleen, 15: testis (highlighted by the red box), and 16: thymus.

(C) *MAP7D3* expression profile throughout human spermatogenesis. Transcript analyses of single-cell RNA quantitative sequencing datasets from human adult testis are available in the literature using the ReproGenomics viewer. Transcript levels are indicated in UMI (unique molecular identifier) normalized for all stages of germ cell differentiation (spermatogonia to differentiated spermatids) and somatic cell types (Leydig cells, Sertoli cells, macrophages).

(D) Left panel: semi-quantitative RT-PCR amplifying *MAP7D3-201* from spermatozoa from the control individual and the patient and normalization against *HPRT*. Middle panel: electropherogram of amplicon sequencing. Right panel: RT-qPCR of patient spermatozoa.

(E) MAP7D3 structure showing the coiled-coil domains (CC), mutation site (red asterisk), and antibody epitope. Immunoblot assay of MAP7D3 from the patient spermatozoa (red asterisk, expected size of MAP7D3). Immunofluorescence assay of MAP7D3 from the patient spermatozoa with tubulin co-staining. Scale bar 10 μm.

We performed semi-quantitative and quantitative RT-PCR assays targeting *MAP7D3* isoforms on a semen sample from the patient. Both analyses showed lower *MAP7D3* transcript levels than in sperm from a control individual, whereas *HPRT* and *GAPDH* transcripts were equally detected (Figure 1D; Table S3), indicative of nonsense-mediated decay of the transcripts. Sequencing of RT-PCR amplicons also confirmed the *c.850 C>T* transition initially identified by whole-exome sequencing and predicted the introduction of a premature stop codon at position p.Gln284. Importantly, we performed immunoblot and immunofluorescence assays using an antibody directed against the C-terminal region of MAP7D3 and detected no signal in the spermatozoa from the patient, in contrast to the control, indicating that the protein was either absent or truncated (Figure 1E). Given the role of MAP proteins in microtubule stabilization, we analyzed the sperm ultrastructure by TEM and observed a slight increase in sections lacking a number of peripheral microtubule doublets (patient: 22%, control mean: 9%; n = 4), whereas the overall axonemal structure was correct (9 + 2 pattern) (Figure S1C). Based on the previously described data and the phenotype of moderate asthenozoospermia reported for MAP7D3-deficient mice, we concluded that the hemizygous *MAP7D3 c.850C>T* (p.Gln284*) variant likely contributed to the patient phenotype but only to a minor degree.

The *IQCH3 c.1456+1G>C* variant affects *IQCH* transcript and protein levels in sperm from the patient

We next characterized the second variant identified by exome sequencing, which corresponds to a homozygous *c.1456+1G>C* substitution in the *IQCH* gene (MIM 612523) and affects the consensus sequence of the splice donor site located in intron 11 (Figure 2A). *IQCH* is located on chromosome 15 and is comprised of 21 exons, encoding a major protein of 1027 amino acids (UniProtKB: Q86VS.3) (Figure 2A). The IQCH major isoform was predicted to contain several enzymatic, metabolic, and signaling domains (carbamate kinase-like domain, Zn-dependent exopeptidase domain, and lactate dehydrogenase C-terminal-like domain), although their functionality was not demonstrated.[20] In addition, IQCH harbors a calmodulin-binding IQ consensus motif previously reported in various signaling proteins.[21] Given the crucial role of calcium and calmodulin in sperm motility and maturation, we considered IQCH to be a strong candidate gene for the asthenozoospermia observed in the patient. Analysis of public databases showed the identified c.1456 + 1G>C variant to be associated with a low allele frequency (gnomAD v2.1.1: 8.8x10-5 in the heterozygous state, chr15:67385020 G>C [GRCh38.p13], rs369043506 (Figure 2A). In addition, in contrast to the ubiquitous expression pattern of MAP7D3, IQCH appears to be preferentially expressed in the testis (Illumina Body Map, The Human Protein Atlas database, ReproGenomics Viewer). Analysis of single-cell RNA sequencing datasets from human adult testis (ReproGenomics viewer,[18]) also showed *IQCH* transcripts in germ cells from the early spermatocyte to late spermatid stages but their near absence from somatic cells (Leydig, Sertoli cells) (see Figure 2C).

IQCH encodes several transcript isoforms due to alternative splicing (Ensembl genome browser); we focused our attention on the three main isoforms (Figure S2A): *IQCH*-201 (4253 bp, 1027 aa), *IQCH*-206 (3112 bp, 684 aa), and *IQCH*-214 (1822 bp, 315 aa). We first assessed their tissue distribution by performing RT-PCR assays on a panel of human tissues. *IQCH-201* and *206*, both comprising the entire functional core, appeared to be mainly expressed in the testis, as well as in lower amounts in the lungs, liver, kidneys, pancreas, ovary, prostate, and spleen (Figure 2B), in accordance with available public data from several databases (Illumina bodyMap2 transcriptome, GTEx portal). *IQCH-214*, the shorter isoform carrying the IQ

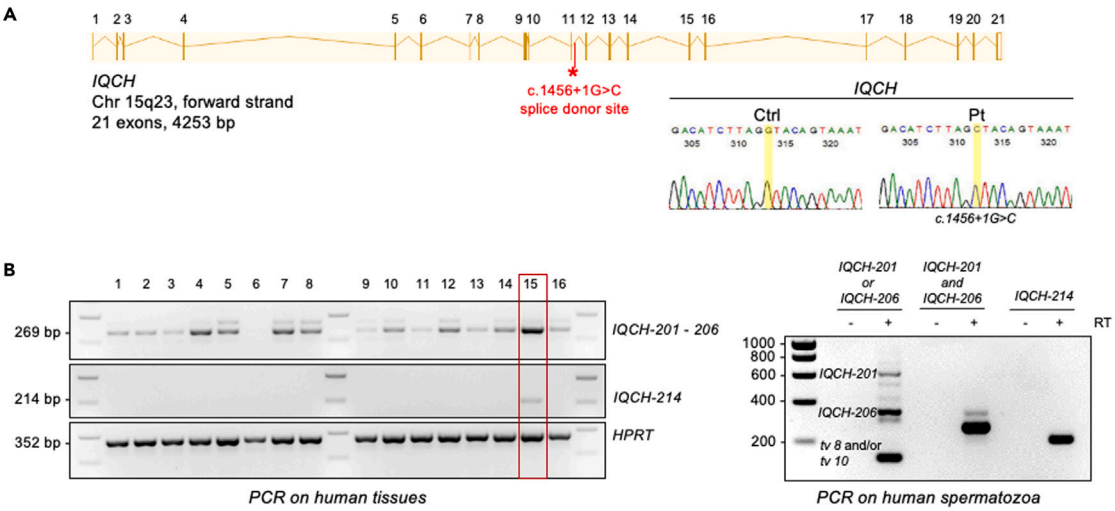
A
IQCH
Chr 15q23, forward strand
21 exons, 4253 bp
c.1456+1G>C
splice donor site
IQCH
Ctrl
Pt
c.1456+1G>C
B
269 bp
214 bp
352 bp
IQCH-201 - 206
IQCH-214
HPRT
PCR on human tissues
IQCH-201 or IQCH-206
IQCH-201 and IQCH-206
IQCH-214
RT
IQCH-201
IQCH-206
tv 8 and/or tv 10
PCR on human spermatozoa

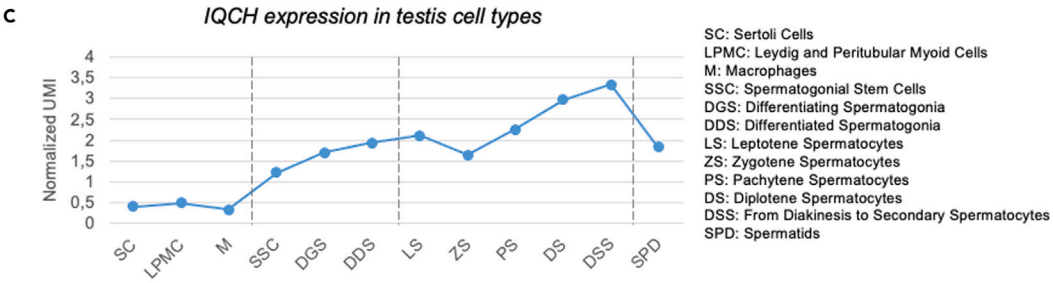
C
IQCH expression in testis cell types
Normalized UMI
SC
LPMC
M
SSC
DGS
DDS
LS
ZS
PS
DS
DSS
SPD
SC: Sertoli Cells
LPMC: Leydig and Peritubular Myoid Cells
M: Macrophages
SSC: Spermatogonial Stem Cells
DGS: Differentiating Spermatogonia
DDS: Differentiated Spermatogonia
LS: Leptotene Spermatocytes
ZS: Zygotene Spermatocytes
PS: Pachytene Spermatocytes
DS: Diplotene Spermatocytes
DSS: From Diakinesis to Secondary Spermatocytes
SPD: Spermatids

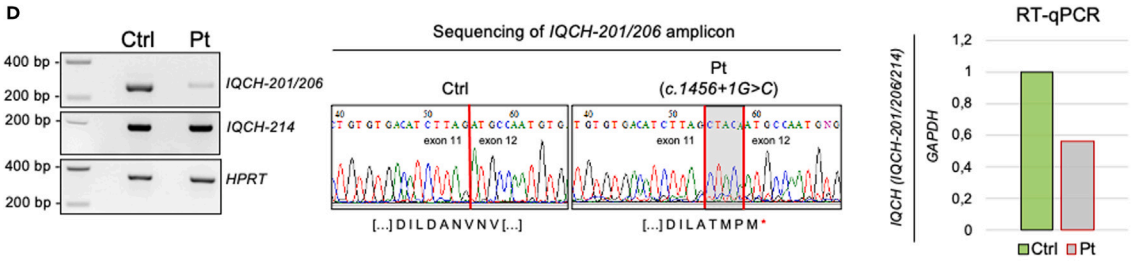
D
Ctrl
Pt
IQCH-201/206
IQCH-214
HPRT
Sequencing of IQCH-201/206 amplicon
Ctrl
Pt (c.1456+1G>C)
exon 11
exon 12
[...]DILDANVNV[...]
[...]DILATMPM*
RT-qPCR
IQCH (IQCH-201/206/214)
GAPDH
Ctrl
Pt

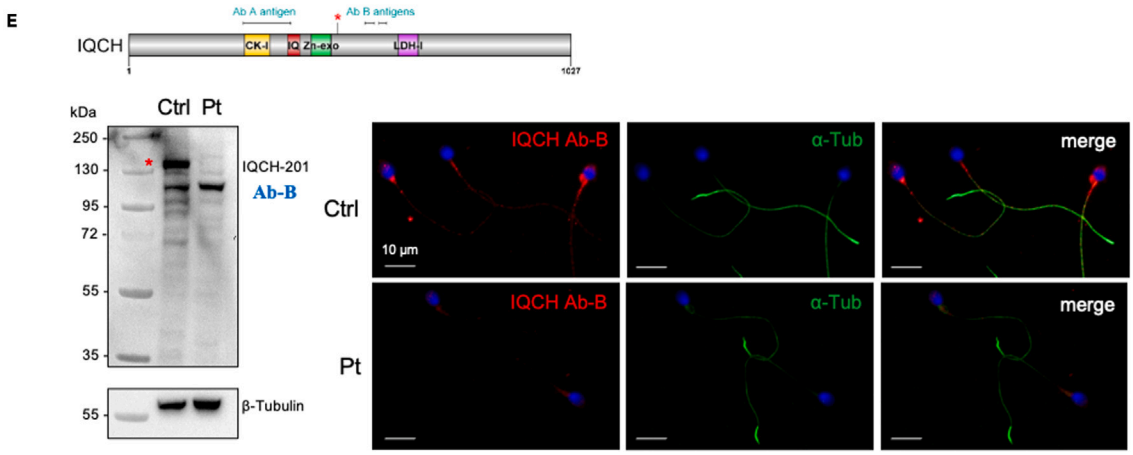
E
Ab A antigen
Ab B antigens
IQCH
CK-I
IQ
Zn-exo
LDH-I
kDa
Ctrl
Pt
IQCH-201
Ab-B
β-Tubulin
IQCH Ab-B
α-Tub
merge
10 µm

Figure 2. Characterization of the *IQCH* homozygous *c.1456+1G>C* variant identified in the patient

(A) Linear structure of the IQCH gene showing exons (bars) and introns (junctions). The red asterisk indicates the mutation site (source: Ensembl genome browser). Chromatograms of IQCH Sanger sequencing for the patient (right) and control individual (left).

(B) Analysis of *IQCH* isoforms in human adult tissues and spermatozoa samples. Samples lacking reverse transcriptase for cDNA amplification (-RT) were used as a negative control. Tissues: 1: heart, 2: brain, 3: placenta, 4: lung, 5: liver, 6: muscle, 7: kidney, 8: pancreas, 9: colon, 10: ovary, 11: leukocytes, 12: prostate, 13: intestine, 14: spleen, 15: testis (highlighted by the red box), and 16: thymus.

(C) IQCH expression profile throughout human spermatogenesis according to single-cell RNA-seq quantitative sequencing (data from the ReproGenomics viewer). Transcript levels are indicated in UMI (unique molecular identifier) normalized for all stages of germ cell differentiation (spermatogonia to differentiated spermatids) and somatic cell type (Leydig cells, Sertoli cells, macrophages).

(D) Left panel: semi-quantitative RT-PCR analysis of *IQCH* isoforms in spermatozoa from the control individual and the patient. The RT-PCR signal was normalized against that of *HPRT* (352 bp amplicon). Middle panel: chromatograms showing the amplicon sequencing, with the red lines marking the exon boundaries. Right panel: RT-qPCR analysis of *IQCH* transcripts in sperm from the control individual and the patient after normalization against *GAPDH*.

(E) Linear structure of the IQCH protein showing multiple enzymatic, metabolic, and signaling domains, together with the mutation site identified in the patient of the present study and the localization of antibody epitopes used in the experimental analyses. *CK-l*, *carbamate kinase-like domain*; *IQ*, *IQ motif*; *Zn-exo*, *Zn-dependent exopeptidase domain*; *LDH-l*, *lactate dehydrogenase C-terminal domain-like* (figure created using DOG software[22]). Western blot and immunodetection analyses of IQCH from spermatozoa from the patient using antibody Ab-B. α-tubulin is stained in green and DNA with DAPI, in blue. Scale bar 10 μm.

motif, was much less abundant and only detectable in the testis. We detected all three transcript isoforms in ejaculated spermatozoa from control individuals (Figure 2B).

We investigated the molecular consequences of the identified variant by performing semi-quantitative RT-PCR analysis on a semen sample from the patient versus that from a control individual using primers located in exons 11 to 12 of *IQCH* and encompassing the mutation site. We observed a noteworthy decrease in the major *IQCH* transcripts in the patient semen, using the housekeeping gene *HPRT* to normalize the results (Figure 2D). Sequencing of the *IQCH* amplicons showed an abnormal splice event in intron 11–12 subsequent to the recognition of a cryptic downstream donor site. This causes the retention of five additional intronic bases in the transcript of the patient, predicted to change the downstream amino acid sequence and generate a premature stop codon at position p.491. The transcript isoform *IQCH-214*, which is not affected by the mutation, was normally detected in both the control and patient spermatozoa (Figure 2D). We confirmed the quantitative alteration of *IQCH* transcripts in spermatozoa from the patient by performing RT-qPCR targeting the whole isoforms, which confirmed a significant decrease in transcript levels in line with nonsense-mediated decay (Figure 2D; Table S3). Consistent with this result, western blot analyses using two available antibodies that target the central region of IQCH (Ab-A and Ab-B) showed the loss of the IQCH-201 isoform in the patient spermatozoa (Figures 2E and S2B). Immunofluorescence staining of the patient spermatozoa using both antibodies also confirmed this result. There was a strong decrease in staining in the flagella, except in the midpiece region, which could correspond to the unaffected short isoform (Figures 2E and S2B). Overall, our data demonstrate that the *IQCH c.1456+1G>C* variant severely impacts IQCH expression and/or localization, and may largely contribute to the patient's phenotype.

The *IQCH c.1456+1G>C* mutation is associated with a lack of capacitation-related protein phosphorylation

We directly tested the functional impact of the *c.1456+1G>C* mutation on sperm capacitation, given the prediction of a calmodulin-binding IQ motif in IQCH by various *in silico* analysis tools (UniProtKB, InterPro) and the essential role of calcium and bicarbonate in activating PKA and calmodulin kinase pathways during this process. We thus incubated spermatozoa from the patient and spermatozoa from control individuals displaying normal semen parameters in capacitating medium for 3 h at 37°C (Ferticult-IVF medium enriched in calcium and bicarbonate, and supplemented with 3% albumin). In spermatozoa from controls individuals, the typical phosphotyrosine protein profile associated with capacitation was observed as illustrated (Figures 3A and S3A). In contrast, spermatozoa from the patient carrying the *IQCH c.1456+1G>C* failed to induce protein phosphorylation during *in vitro* capacitation (Figure 3A), indicating a dysregulation of the signaling pathways normally triggered by ion fluxes during capacitation. The analysis of spermatozoa from four other infertile patients displaying asthenozoospermia often associated with reduced sperm viability (Table S4) showed the induction of normal protein phosphorylation profile during capacitation (Figure S3B). This indicates that the lack of protein phosphorylation is not a common feature associated with functional asthenozoospermia but is related to the *IQCH c.1456+1G>C* variant. Lastly, since hypotonic challenge was shown to increase sperm tail coiling and folding in a dose-response pattern[23] and that calcium participates in the regulation of sperm cell volume,[24] we sought to analyze the functional sensitivity of

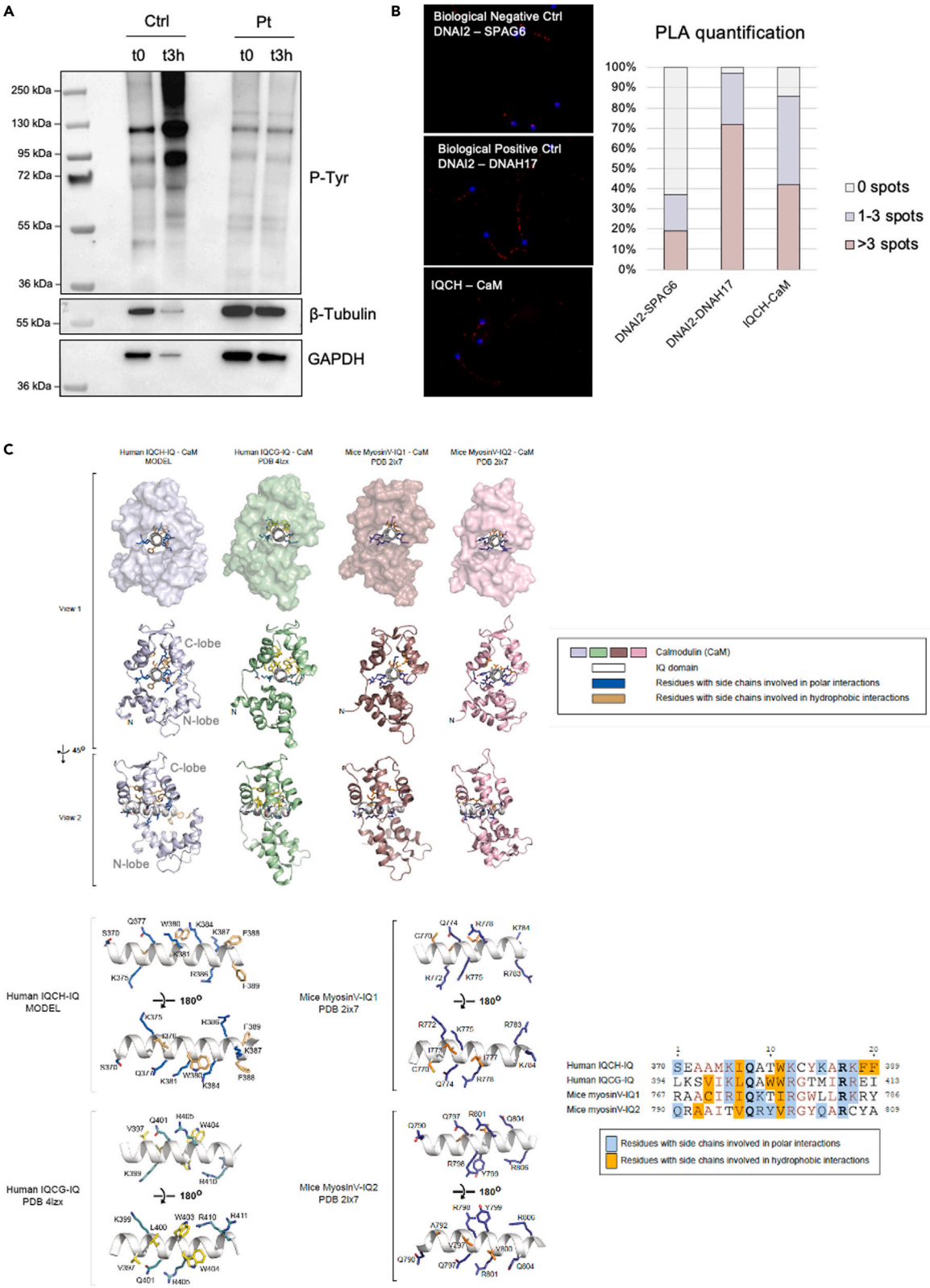
A
Ctrl
Pt
t0
t3h
t0
t3h
250 kDa
130 kDa
95 kDa
72 kDa
55 kDa
36 kDa
55 kDa
36 kDa
P-Tyr
β-Tubulin
GAPDH
B
Biological Negative Ctrl
DNAI2 – SPAG6
Biological Positive Ctrl
DNAI2 – DNAH17
IQCH – CaM
PLA quantification
100%
90%
80%
70%
60%
50%
40%
30%
20%
10%
0%
DNAI2-SPAG6
DNAI2-DNAH17
IQCH-CaM
0 spots
1-3 spots
>3 spots
C
Human IQCH-IQ - CaM
MODEL
Human IQCG-IQ - CaM
PDB 4lzx
Mice MyosinV-IQ1 - CaM
PDB 2lx7
Mice MyosinV-IQ2 - CaM
PDB 2lx7
View 1
C-lobe
N-lobe
45°
View 2
C-lobe
N-lobe
Calmodulin (CaM)
IQ domain
Residues with side chains involved in polar interactions
Residues with side chains involved in hydrophobic interactions
Human IQCH-IQ
MODEL
Mice MyosinV-IQ1
PDB 2lx7
180°
Human IQCG-IQ
PDB 4lzx
Mice MyosinV-IQ2
PDB 2lx7
180°
Human IQCH-IQ 370 SEAAMKIQATWKCYKARKFF 389
Human IQCG-IQ 394 LKSVIKLQAWWRGTMIRREI 413
Mice myosinV-IQ1 767 RAACIRIQKTIRGWLLRKRY 786
Mice myosinV-IQ2 790 QRAAITVQRYVRGYQARCYA 809
Residues with side chains involved in polar interactions
Residues with side chains involved in hydrophobic interactions

Figure 3. Association of IQCH with calmodulin in flagella and its requirement for sperm capacitation

(A) Western blot analysis of protein tyrosine phosphorylation following *in vitro* capacitation of spermatozoa from the patient and a control individual, at 37°C for 3 h. The data presented for the control individual are representative of the profiles obtained with semen samples from five control individuals displaying normal semen parameters following WHO criteria (Figure S3A).

(B) Assessment of the IQCH/calmodulin interaction by proximity ligation assay (PLA). Analysis of the physical proximity of IQCH and calmodulin (CaM) relative to the biological negative control (DNAI2-SPAG6, two proteins from different axonemal complexes) and positive control (DNAI2-DNAH17, two proteins from the same axonemal complex).

(C) 3D structures of IQ motifs bound to calmodulin in the calcium free status. Side chains of the residues involved in IQ-CaM interactions are shown as sticks and colored blue or orange for polar and hydrophobic contacts, respectively. Structural and sequence alignments of the IQ motifs from IQCH, IQCG, and Myosin V are shown.

the patient sperm cells to changes in environmental ion content. Sperm cells from the patient were subjected to density gradient centrifugation in capacitating medium enriched in calcium. We observed an increase in coiled flagella after gradient selection (21%→43%; data not shown), indicating a non-constitutional origin of this morphological abnormality and higher susceptibility to osmotic stress, consistent with a deregulation of the calcium-dependent signaling pathways.

IQCH is a calmodulin-associated protein

We next assessed the physical and functional interaction of IQCH with calmodulin. We first performed a proximity ligation assay (PLA), which allows *in situ* visualization of protein complexes and interactions in the range of 40 nm (Figure 3B). We used DNAI2 and DNAH17 (two components of the same flagellar axoneme structure, the outer dynein arms) as a positive control and DNAI2 and SPAG6 (SPAG6 being a component of the central pair complex) as a negative control. We quantified 97% and 37% of stained flagella for the positive and negative controls, respectively. In parallel, the quantification of IQCH and calmodulin proximity showed 86% stained spermatozoa, consistent with a physical interaction between IQCH and calmodulin.

To provide further evidence of an IQCH-calmodulin association, we used AlphaFold to predict the structure of the complex formed by the IQ motif of human IQCH and calmodulin-1 in the calcium-free form (Apo-CaM) and then compared this model with published experimental crystal structures of IQ-CaM complexes involving IQCG and myosin V proteins.[25,26] The IQ helix was positioned between the N- and C-terminal lobes of calmodulin, mostly interacting with the C-lobe, in both the IQCH-CaM model and established structures from crystals (see Figure 3C). The module formed by the IQ motif and the CaM C-lobe adopted a highly similar conformation in all analyzed structures, whereas the relative orientation of the CaM N-lobe was more variable. We identified the residues and side chains involved in the interaction in each structure, for which the network was highly conserved. Indeed, the top of the IQ helix tends to form hydrophobic contacts, whereas the sides of the helix tend to make polar contacts (Figure 3C, views 1 and 2). A closer analysis of the interface shows a conserved mode of interaction between the IQ motif and calmodulin (Figure 3C). The IQ consensus motif [FILV]Qxxx[RK]Gxxx[RK]xx[FILVWY] mediating the calmodulin interaction is characterized by a first variable residue carrying a hydrophobic chain (isoleucine, phenylalanine, leucine, or valine), followed by a fixed glutamine residue surrounded by charged residues (arginine, lysine) or other hydrophobic chains at specific positions. We found the residues engaged in polar and hydrophobic interactions at similar positions in the various IQ domains we analyzed, shown by structural and sequence alignments (Figure 3C). Overall, our data indicate that the IQ motif of IQCH interacts with calmodulin, adopting a binding mode similar to that of previously described IQ-CaM complexes,[25,26] and are consistent with a role of IQCH in the calmodulin-dependent signaling pathways required for sperm capacitation and fertilization potential.

IQCH shows a helicoidal spatial distribution around the sperm axoneme

We next used high-resolution microscopy and performed co-immunostaining of IQCH with α-tubulin and calmodulin to better define the subcellular localization of IQCH within the sperm flagellum. Using both STORM and STED microscopy, we first observed IQCH to be located around the microtubular axoneme and to adopt a peculiar helical distribution relative to the continuous axonemal staining observed for tubulin (Figures 4A and S4). An estimation of the IQCH helicoidal periodicity suggests an interval of approximatively 150 nm and a helical pitch of approximately 400–500 nm based on the signal peaks (Figure 4B). In addition, analysis of the co-staining of IQCH and calmodulin showed calmodulin staining to appear as a uniform and compact signal at the center of the sperm flagellum surrounded by the helicoidal IQCH staining. These observations are consistent with previously reported data for protist flagella

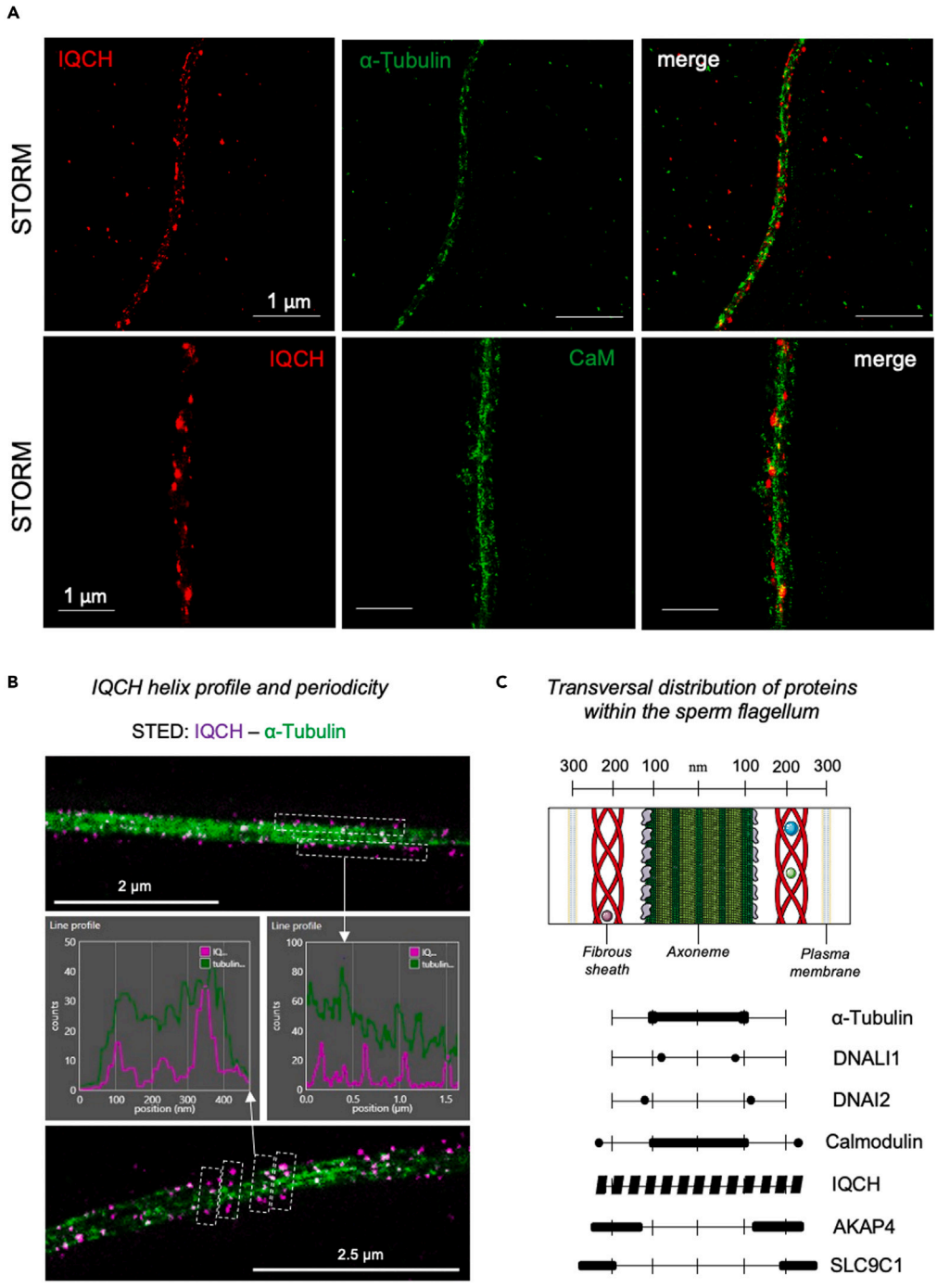

Figure 4. Analysis of the spatial distribution of IQCH within sperm flagella by super-resolution microscopy

(A) STORM imaging of sperm flagella stained for IQCH (red) and α-tubulin (green) or calmodulin (CaM, green). Scale bars 1 µm.

(B) STED images of co-staining IQCH (violet) and α-tubulin (green), highlighting the helicoidal spatial distribution of IQCH along the sperm flagellum (dashed frames) and its co-localization with calmodulin. Distribution profiles of the signal in the selected regions highlight the longitudinal and transversal periodicity of IQCH. Scale bars 2 µm and 2.5 µm.

(C) Schematic representation of a transversal section of a sperm flagellum with the localization of proteins identifying the various complexes and subcellular regions of sperm flagella localization [Graphical elements from Servier Medical Art, licensed under a Creative Commons Attribution 3.0 Unported License]. Distribution data were obtained by analyzing the STORM and STED images shown in Figure S4.

indicating that a calmodulin ortholog (RSP20) is a component of a multiprotein complex tightly associated with the base of the radial spokes (i.e., the calmodulin- and spoke-associated complex) and mediates the calcium-dependent regulation of dynein activity.[27,28] Interestingly, we also detected calmodulin, but not IQCH, at the flagellar periphery, compatible with a sub-membranous cytoplasmic pool, which could support functional proximity to plasma membrane calcium channels (Figure 4A,[29]). In order to support our experimental results regarding IQCH and calmodulin, we similarly analyzed previously described axonemal, peri-axonemal, and plasma membrane markers: DNAI2 for the outer dynein arms, DNALI1 for the inner dynein arms, AKAP4 for the fibrous sheath, and SLC9C1 for the plasma membrane (Figure S4). For each condition, the signal distribution across the sperm flagellum was recorded and measured to establish the comparative spatial distribution of the proteins (Figure 4C). All analyzed markers localized to the expected range of lateral distribution, consistent with published data.[30,31] IQCH staining was disseminated throughout the transversal flagellar section, in accordance with the observed longitudinal and helical profile. Such intriguing distribution pattern could be related to the multiple predicted enzymatic domains, and should be further investigated to precise the regulatory functions of IQCH during sperm capacitation.

DISCUSSION

Among the various male infertility phenotypes, asthenozoospermia (i.e., absent or reduced sperm motility) appears to be the most frequent.[32] Asthenozoospermia is often associated with a reduced number of spermatozoa and/or the presence of sperm morphological defects. The MMAF phenotype, characterized by severe disorganization of the flagellar structure, is illustrative of this condition and has been the subject of exhaustive genetic investigations over the last five years (for reviews[33–35]). By contrast, only a few genes responsible for isolated functional asthenozoospermia have been identified to date. Most of them encode ion channels and transporters that regulate the downstream signaling pathways required for sperm motility and capacitation (review[12]).

Here, we identified and characterized the sperm of an infertile patient presenting asthenozoospermia with a hemizygous truncating variant in *MAP7D3*, an X-linked gene encoding a tubulin-associated protein, together with a rare homozygous splice variant affecting the long isoform of *IQCH*, which encodes a protein of unknown function harboring a calmodulin-binding IQ motif. We demonstrate the deleterious effects of both variants, supporting their contribution to the patient phenotype with cumulative effects. Given the phenotype of moderate asthenozoospermia described for MAP7D3-deficient mice,[17] we assume that this variant also affects sperm motility in humans, possibly by altering microtubule stability within the flagellar axoneme. We also provide strong evidence that the *IQCH* variant is associated with an impairment of calmodulin-mediated phosphorylation pathways. As only the long protein isoform of IQCH was affected by the variant, the potential conservation of the short IQCH-214 isoform could explain the absence of total asthenozoospermia observed in the present case. These results are of interest in the field of the genetics of male infertility, as, to date, the contribution of multiple gene variants to this condition has never been thoroughly investigated relative to other pathologies.[36,37] Only one recent study has presented the combined effect of additional heterozygous mutations in mice, resulting in asthenozoospermia due to the MMAF phenotype and supporting the hypothesis of oligogenism in the context of male infertility.[38] The case that we have described therefore highlights the need to explore and better characterize how complex genotypes with multiple hetero/homozygous variants, each having a moderate individual impact, can result in pathological conditions.

Overall, our study identifies IQCH as a partner of calmodulin, a well-established calcium sensor acting as an intracellular messenger to mediate various biological functions. Several calmodulin antagonists were previously shown to inhibit sperm capacitation *in vitro*,[39,40] in particular by preventing protein tyrosine phosphorylation of several sperm components.[40] In line with these results, we show that *IQCH* mutation is associated with a lack of capacitation-associated protein phosphorylation in sperm cells from the patient. It is likely that IQCH could act as a target of the calmodulin-Ca^{2+} complex by recruiting and/or activating downstream kinases; this could be mediated by the carboxy-terminal region only present in IQCH long isoform, and which we found to be impacted by the mutation. Supporting this hypothesis, immunoprecipitation and mass spectrometry analyses performed in HEK293 human cell line have identified IQCH as a partner of NEK4,[41] a kinase preferentially expressed in the human testis (EMBL-EBI Expression atlas, Human protein atlas) and abundant in the germ cells throughout all stages of spermatogenesis (ReproGenomics viewer;[18]). Further studies to identify additional protein partners in the sperm cells and characterize other IQCH

predicted metabolic and enzymatic domains would help in better defining its functions and regulatory mechanisms at the intersection between calcium signaling and sperm bioenergetics.

Limitations of the study

We have described the case of an infertile patient presenting asthenozoospermia and carrying truncating mutations in two genes: *MAP7D3* and *IQCH*. By using semen samples from the patient, we demonstrated that both mutations are pathogenic at the transcript and protein levels. However, our study reports a single patient and the analysis of additional patients will be required to define the prevalence of these mutations in human asthenozoospermia. Besides, the relevance of these two genes for sperm motility and fertilization potential is supported by data from the literature together with *in silico* and *in vitro* experiments we provided in here. In particular, we show a failure of sperm capacitation for the mutated patient, in contrast to other patients displaying idiopathic asthenozoospermia. This suggests the involvement of IQCH in sperm motility and capacitation possibly by interacting with calmodulin, but further experimentations are needed to clearly demonstrate the function of IQCH and to identify the associated molecular mechanisms.

STAR★METHODS

Detailed methods are provided in the online version of this paper and include the following:

- KEY RESOURCES TABLE
- RESOURCE AVAILABILITY
  - Lead contact
  - Materials availability
  - Data and code availability
- EXPERIMENTAL MODEL AND STUDY PARTICIPANT DETAILS
  - Subjects
  - Human semen samples
- METHOD DETAILS
  - Transmission electron microscopy analysis
  - Whole exome sequence analysis
  - Sanger sequencing
  - RT-PCR and RT-qPCR analyses
  - Immunofluorescence assay
  - Western-blot analysis
  - Super-resolution microscopy
  - Proximity ligation assay
  - Structural modelling
  - Capacitation assay
- QUANTIFICATION AND STATISTICAL ANALYSIS
  - Super resolution microscopy data analysis

SUPPLEMENTAL INFORMATION

Supplemental information can be found online at https://doi.org/10.1016/j.isci.2023.107354.

ACKNOWLEDGMENTS

We thank all the individuals included in this study for their cooperation, as well as all the referring physicians. We also thank all the technicians from the *Service de Biologie de la Reproduction* at the Hospital Cochin (Paris) for the routine semen sample evaluation (Jacques Bras, Nathalie Chériau, Véronique Hernandorena, Jean-Claude Cambronne, and Caroline Villalon). Finally, we thank the Cellular Imaging Facility of the Institut Cochin (Jean-Marc Massé, Alain Schmitt,and Azzedine Yacia) for electron microscopy procedures, the IMAG'IC platform of the Institut Cochin (Pierre Bourdoncle), and the MicroCell platform of the Institute for Advanced Biosciences (Mylène Pezet) for their assistance in the super-resolution microscopy.

Funding: This work was supported by the Institut National de la Santé et de la Recherche Médicale (INSERM), the Centre National de la Recherche Scientifique (CNRS), the Université Paris Descartes, the University Grenoble-Alpes, and the French National Research Agency (Grant SPERMetabo ANR-21-CE14-0070 to A.T.; grant FLAGEL-OME ANR-19-CE17-0014 to P.R., N.T.M., and A.T.; grant ANR-21-CE18-0041 to JG).

AUTHOR CONTRIBUTIONS

A.T. designed the study. E.D. and C.P. recruited the patient and performed the clinical analysis and characterization. Z.-E.K., C.C., N.T.-M., and P.F.R. performed the exome and bioinformatics analysis. C.Caz performed the genomic validation of the variants. E.C. performed the experimental work (RT-PCR, RT-qPCR, sequencing, immunofluorescence, immunoblotting, STORM & STED, PLA assay) and data quantification and analyses. C.S. and J.G. performed *in silico* protein interaction modeling. E.E.K. and A.T. performed the TEM analyses. A.T. performed sperm capacitation assays. P.L., L.S., and M.W. helped with establishing the experimental conditions. E.C. and A.T. made the illustrations. E.C., M.W., and A.T. analyzed the data. E.C. and A.T. wrote the manuscript. M.W. and E.D. critically read the manuscript. All authors have read and approved the manuscript.

DECLARATION OF INTERESTS

The authors declare no conflict of interest.

INCLUSION AND DIVERSITY

We support inclusive, diverse, and equitable conduct of research. We worked to ensure ethnic or other types of diversity in the recruitment of human subjects. One or more of the authors of this paper self-identifies as an underrepresented ethnic minority in their field of research or within their geographical location.

Received: April 4, 2023
Revised: May 23, 2023
Accepted: July 7, 2023
Published: July 10, 2023

REFERENCES

1. Mortimer, D. (2018). The functional anatomy of the human spermatozoon: relating ultrastructure and function. Mol. Hum. Reprod. *24*, 567–592. https://doi.org/10.1093/molehr/gay040.

2. Austin, C.R. (1951). Observations on the penetration of the sperm in the mammalian egg. Aust. J. Sci. Res. B. *4*, 581–596. https://doi.org/10.1071/bi9510581.

3. Chang, M.C. (1951). Fertilizing Capacity of Spermatozoa deposited into the Fallopian Tubes. Nature *168*, 697–698. https://doi.org/10.1038/168697b0.

4. Dey, S., Brothag, C., and Vijayaraghavan, S. (2019). Signaling Enzymes Required for Sperm Maturation and Fertilization in Mammals. Front. Cell Dev. Biol. *7*, 341. https://doi.org/10.3389/fcell.2019.00341.

5. Gervasi, M.G., and Visconti, P.E. (2017). Molecular changes and signaling events occurring in spermatozoa during epididymal maturation. Andrology *5*, 204–218. https://doi.org/10.1111/andr.12320.

6. Mahé, C., Zlotkowska, A.M., Reynaud, K., Tsikis, G., Mermillod, P., Druart, X., Schoen, J., and Saint-Dizier, M. (2021). Sperm migration, selection, survival, and fertilizing ability in the mammalian oviduct. Biol. Reprod. *105*, 317–331. https://doi.org/10.1093/biolre/ioab105.

7. Freitas, M.J., Vijayaraghavan, S., and Fardilha, M. (2017). Signaling mechanisms in mammalian sperm motility. Biol. Reprod. *96*, 2–12. https://doi.org/10.1095/biolreprod.116.144337.

8. Gervasi, M.G., and Visconti, P.E. (2016). Chang's meaning of capacitation: A molecular perspective. Mol. Reprod. Dev. *83*, 860–874. https://doi.org/10.1002/mrd.22663.

9. Castillo, J., Bogle, O.A., Jodar, M., Torabi, F., Delgado-Dueñas, D., Estanyol, J.M., Ballescà, J.L., Miller, D., and Oliva, R. (2019). Proteomic Changes in Human Sperm During Sequential in vitro Capacitation and Acrosome Reaction. Front. Cell Dev. Biol. *7*, 295. https://doi.org/10.3389/fcell.2019.00295.

10. Puga Molina, L.C., Luque, G.M., Balestrini, P.A., Marín-Briggiler, C.I., Romarowski, A., and Buffone, M.G. (2018). Molecular Basis of Human Sperm Capacitation. Front. Cell Dev. Biol. *6*, 72. https://doi.org/10.3389/fcell.2018.00072.

11. Brown, S.G., Publicover, S.J., Barratt, C.L.R., and Martins da Silva, S.J. (2019). Human sperm ion channel (dys)function: implications for fertilization. Hum. Reprod. Update *25*, 758–776. https://doi.org/10.1093/humupd/dmz032.

12. Cavarocchi, E., Whitfield, M., Saez, F., and Touré, A. (2022). Sperm Ion Transporters and Channels in Human Asthenozoospermia: Genetic Etiology, Lessons from Animal Models, and Clinical Perspectives. Int. J. Mol. Sci. *23*, 3926. https://doi.org/10.3390/ijms23073926.

13. Wang, H., McGoldrick, L.L., and Chung, J.-J. (2021). Sperm ion channels and transporters in male fertility and infertility. Nat. Rev. Urol. *18*, 46–66. https://doi.org/10.1038/s41585-020-00390-9.

14. Chemes, H.E., Brugo, S., Zanchetti, F., Carrere, C., and Lavieri, J.C. (1987). Dysplasia of the fibrous sheath: an ultrastructural defect of human spermatozoa associated with sperm immotility and primary sterility**Supported by grant 0934 from Consejo Nacional de Investigaciones Científicas y Técnicas. Fertil. Steril. *48*, 664–669. https://doi.org/10.1016/S0015-0282(16)59482-5.

15. Escalier, D. (2006). Arrest of flagellum morphogenesis with fibrous sheath immaturity of human spermatozoa. Andrologia *38*, 54–60. https://doi.org/10.1111/j.1439-0272.2006.00711.x.

16. Sun, X., Shi, X., Liu, M., Li, D., Zhang, L., Liu, X., and Zhou, J. (2011). Mdp3 is a novel microtubule-binding protein that regulates microtubule assembly and stability. Cell Cycle *10*, 3929–3937. https://doi.org/10.4161/cc.10.22.18106.

17. Lu, C., Zhang, Y., Qin, Y., Xu, Q., Zhou, R., Cui, Y., Zhu, Y., Zhang, X., Zhang, J., Wei, X., et al. (2020). Human X chromosome exome sequencing identifies *BCORL1* as contributor to spermatogenesis. J. Med. Genet. *58*, 56–65. https://doi.org/10.1136/jmedgenet-2019-106598.

18. Wang, M., Liu, X., Chang, G., Chen, Y., An, G., Yan, L., Gao, S., Xu, Y., Cui, Y., Dong, J., et al. (2018). Single-Cell RNA Sequencing Analysis Reveals Sequential Cell Fate Transition during Human Spermatogenesis. Cell Stem Cell *23*, 599–614.e4. https://doi.org/10.1016/j.stem.2018.08.007.

19. Wang, L., Yan, M., Wong, C.K.C., Ge, R., Wu, X., Sun, F., and Cheng, C.Y. (2021).

Microtubule-associated proteins (MAPs) in microtubule cytoskeletal dynamics and spermatogenesis. Histol. Histopathol. *36*, 249–265. https://doi.org/10.14670/HH-18-279.

20. Yin, L.-L., Li, J.-M., Zhou, Z.-M., and Sha, J.-H. (2005). Identification of a novel testis-specific gene and its potential roles in testis development/spermatogenesis. Asian J. Androl. *7*, 127–137. https://doi.org/10.1111/j.1745-7262.2005.00041.x.

21. Bähler, M., and Rhoads, A. (2002). Calmodulin signaling via the IQ motif. FEBS Lett. *513*, 107–113. https://doi.org/10.1016/S0014-5793(01)03239-2.

22. Ren, J., Wen, L., Gao, X., Jin, C., Xue, Y., and Yao, X. (2009). DOG 1.0: illustrator of protein domain structures. Cell Res. *19*, 271–273. https://doi.org/10.1038/cr.2009.6.

23. Holmes, E., Björndahl, L., and Kvist, U. (2020). Hypotonic challenge reduces human sperm motility through coiling and folding of the tail. Andrologia *52*, e13859. https://doi.org/10.1111/and.13859.

24. Pereira, R., Sá, R., Barros, A., and Sousa, M. (2017). Major regulatory mechanisms involved in sperm motility. Asian J. Androl. *19*, 05–14. https://doi.org/10.4103/1008-682X.167716.

25. Chen, L.-T., Liang, W.-X., Chen, S., Li, R.-K., Tan, J.-L., Xu, P.-F., Luo, L.-F., Wang, L., Yu, S.-H., Meng, G., et al. (2014). Functional and molecular features of the calmodulin-interacting protein IQCG required for haematopoiesis in zebrafish. Nat. Commun. *5*, 3811. https://doi.org/10.1038/ncomms4811.

26. Houdusse, A., Gaucher, J.-F., Krementsova, E., Mui, S., Trybus, K.M., and Cohen, C. (2006). Crystal structure of apo-calmodulin bound to the first two IQ motifs of myosin V reveals essential recognition features. Proc. Natl. Acad. Sci. USA *103*, 19326–19331. https://doi.org/10.1073/pnas.0609436103.

27. Smith, E.F. (2002). Regulation of Flagellar Dynein by Calcium and a Role for an Axonemal Calmodulin and Calmodulin-dependent Kinase. MBoC *13*, 3303–3313. https://doi.org/10.1091/mbc.e02-04-0185.

28. Viswanadha, R., Sale, W.S., and Porter, M.E. (2017). Ciliary Motility: Regulation of Axonemal Dynein Motors. Cold Spring Harbor Perspect. Biol. *9*, a018325. https://doi.org/10.1101/cshperspect.a018325.

29. Chung, J.-J., Shim, S.-H., Everley, R.A., Gygi, S.P., Zhuang, X., and Clapham, D.E. (2014). Structurally Distinct Ca2+ Signaling Domains of Sperm Flagella Orchestrate Tyrosine Phosphorylation and Motility. Cell *157*, 808–822. https://doi.org/10.1016/j.cell.2014.02.056.

30. Gu, N.-H., Zhao, W.-L., Wang, G.-S., and Sun, F. (2019). Comparative analysis of mammalian sperm ultrastructure reveals relationships between sperm morphology, mitochondrial functions and motility. Reprod. Biol. Endocrinol. *17*, 66. https://doi.org/10.1186/s12958-019-0510-y.

31. Miller, M.R., Kenny, S.J., Mannowetz, N., Mansell, S.A., Wojcik, M., Mendoza, S., Zucker, R.S., Xu, K., and Lishko, P.V. (2018). Asymmetrically Positioned Flagellar Control Units Regulate Human Sperm Rotation. Cell Rep. *24*, 2606–2613. https://doi.org/10.1016/j.celrep.2018.08.016.

32. Heidary, Z., Saliminejad, K., Zaki-Dizaji, M., and Khorram Khorshid, H.R. (2020). Genetic aspects of idiopathic asthenozoospermia as a cause of male infertility. Hum. Fertil. *23*, 83–92. https://doi.org/10.1080/14647273.2018.1504325.

33. Nsota Mbango, J.-F., Coutton, C., Arnoult, C., Ray, P.F., and Touré, A. (2019). Genetic causes of male infertility: snapshot on morphological abnormalities of the sperm flagellum. Basic Clin. Androl. *29*, 2. https://doi.org/10.1186/s12610-019-0083-9.

34. Touré, A., Martinez, G., Kherraf, Z.-E., Cazin, C., Beurois, J., Arnoult, C., Ray, P.F., and Coutton, C. (2021). The genetic architecture of morphological abnormalities of the sperm tail. Hum. Genet. *140*, 21–42. https://doi.org/10.1007/s00439-020-02113-x.

35. Wang, W.-L., Tu, C.-F., and Tan, Y.-Q. (2020). Insight on multiple morphological abnormalities of sperm flagella in male infertility: what is new? Asian J. Androl. *22*, 236–245. https://doi.org/10.4103/aja.aja_53_19.

36. Kelly, M., and Semsarian, C. (2009). Multiple Mutations in Genetic Cardiovascular Disease: A Marker of Disease Severity? Circ. Cardiovasc. Genet. *2*, 182–190. https://doi.org/10.1161/CIRCGENETICS.108.836478.

37. Tada, H., Nohara, A., and Kawashiri, M.A. (2019). Monogenic, polygenic, and oligogenic familial hypercholesterolemia. Curr. Opin. Lipidol. *30*, 300–306. https://doi.org/10.1097/MOL.0000000000000609.

38. Martinez, G., Coutton, C., Loeuillet, C., Cazin, C., Muroňová, J., Boguenet, M., Lambert, E., Dhellemmes, M., Chevalier, G., Hograindleur, J.-P., et al. (2022). Oligogenic heterozygous inheritance of sperm abnormalities in mouse. Elife *11*, e75373. https://doi.org/10.7554/eLife.75373.

39. Navarrete, F.A., García-Vázquez, F.A., Alvau, A., Escoffier, J., Krapf, D., Sánchez-Cárdenas, C., Salicioni, A.M., Darszon, A., and Visconti, P.E. (2015). Biphasic Role of Calcium in Mouse Sperm Capacitation Signaling Pathways. J. Cell. Physiol. *230*, 1758–1769. https://doi.org/10.1002/jcp.24873.

40. Zeng, H.-T., and Tulsiani, D.R.P. (2003). Calmodulin antagonists differentially affect capacitation-associated protein tyrosine phosphorylation of mouse sperm components. J. Cell Sci. *116*, 1981–1989. https://doi.org/10.1242/jcs.00396.

41. Basei, F.L., Meirelles, G.V., Righetto, G.L., dos Santos Migueleti, D.L., Smetana, J.H.C., and Kobarg, J. (2015). New interaction partners for Nek4.1 and Nek4.2 isoforms: from the DNA damage response to RNA splicing. Proteome Sci. *13*, 11. https://doi.org/10.1186/s12953-015-0065-6.

42. Schneider, C.A., Rasband, W.S., and Eliceiri, K.W. (2012). NIH Image to ImageJ: 25 years of Image Analysis. Nat. Methods. *9*, 671–675. https://doi.org/10.1038/nmeth.2089.

43. Jumper, J., Evans, R., Pritzel, A., Green, T., Figurnov, M., Ronneberger, O., Tunyasuvunakool, K., Bates, R., Žídek, A., Potapenko, A., et al. (2021). Highly accurate protein structure prediction with AlphaFold. Nature *596*, 583–589. https://doi.org/10.1038/s41586-021-03819-2.

44. World Health Organization (2021). WHO Laboratory Manual for the Examination and Processing of Human Semen (World Health Organization).

45. Schmittgen, T.D., and Livak, K.J. (2008). Analyzing real-time PCR data by the comparative C(T) method. Nat. Protoc. *3*, 1101–1108. https://doi.org/10.1038/nprot.2008.73.

46. Google Colaboratory (2021). https://colab.research.google.com/github/deepmind/alphafold/blob/main/notebooks/AlphaFold.ipynb.

STAR★METHODS

KEY RESOURCES TABLE

REAGENT or RESOURCE	SOURCE	IDENTIFIER
Antibodies		
rabbit polyclonal anti-IQCH antibody	Sigma-Aldrich	HPA040845; RRID:AB_10672898
rabbit polyclonal anti-IQCH home-made antibody	ProteoGenix	/
rabbit polyclonal anti-MAP7D3	Sigma-Aldrich	HPA035598; RRID:AB_10671108
mouse monoclonal anti-α-Tubulin	Sigma-Aldrich	T9026; RRID:AB_477593
mouse monoclonal anti-Calmodulin antibody	Upstate	05-173; RRID:AB_309644
mouse monoclonal anti-DNAI2 antibody	Abnova	H00064446-M01; RRID:AB_426059
polyclonal mouse anti-DNALI1 antibody	Sigma-Aldrich	SAB1406631; RRID:AB_10740960
rabbit polyclonal anti-AKAP4 antibody	Sigma-Aldrich	HPA020046; RRID:AB_1844693
rabbit polyclonal anti-SLC9C1 antibody	Invitrogen	PA5-104160; RRID:AB_2853488
rabbit polyclonal anti-SPAG6 antibody	Sigma-Aldrich	HPA038440; RRID:AB_10671742
rabbit polyclonal anti- DNAH17 antibody	Sigma-Aldrich	HPA024354; RRID:AB_1847911
mouse monoclonal anti-β-Tubulin clone AA2	Sigma-Aldrich	05-661; RRID:AB_309885
rabbit polyclonal anti-GAPDH antibody	CusAb	PA00025A0Rb
mouse monoclonal anti-phosphotyrosine antibody, clone 4G10	Sigma-Aldrich	05-321; RRID:AB_2891016
goat polyclonal anti-rabbit IgG Alexa Fluor 568	Invitrogen	A-11029; RRID:AB_2534088
goat polyclonal anti-mouse IgG Alexa Fluor 488	Invitrogen	A-28175; RRID:AB_2536161
goat anti-rabbit Alexa Fluor 555	Thermo Fisher Scientific	A-21430; RRID:AB_2535851
goat anti-mouse Alexa Fluor 647	Thermo Fisher Scientific	A-21237; RRID:AB_2535806
goat polyclonal anti-rabbit IgG Abberior STAR 635P	Sigma-Aldrich	53399; RRID:AB_2893229
goat polyclonal anti-mouse IgG Abberior STAR 580	Sigma-Aldrich	52403; RRID:AB_2923543
rabbit polyclonal anti-mouse Ig coupled to Horse Radish Peroxydase (HRP)	Dako	P0260; RRID:AB_2636929
swine polyclonal anti-rabbit Ig coupled to HRP	Dako	P0217; RRID:AB_2728719
Biological samples		
Human spermatozoa from patient and control individuals	/	/
human MTC panels I & II	Clontech Laboratories	636743
Chemicals, peptides, and recombinant proteins		
M2 medium	Sigma-Aldrich	MR-015
Complete EDTA-free Protease Inhibitor cocktail	Sigma-Aldrich	11836170001
Glutaraldehyde solution, Grade I	Sigma-Aldrich	G5882
Paraformaldehyde 16% solution, EM Grade	Electron Microscopy Sciences	15710
Everspark	Idylle	/
Prolong Gold w/o DAPI buffer	Thermo Fisher Scientific	P36930
Vectashield Antifade Mounting Medium with DAPI	Vector Laboratories	H-1200-10
Antigen Unmasking Solution, Citrate-Based	Vector Laboratories	H-3300-250
Ferticult flushing medium with phenol red	FertiPro	FLUSH020PHR
BSA fatty acids-free	Sigma-Aldrich	A8806
Fetal Bovine Serum, qualified	Life Technologies	26140079
Penicillin-streptomycin	Sigma-Aldrich	P4333
PhosSTOP	Roche	4906845001

(*Continued on next page*)

Continued

REAGENT or RESOURCE	SOURCE	IDENTIFIER
WesternBright ECL HRP Substrate	Advansta	K-12045-D50
DMEM, high glucose, GlutaMAX™ Supplement	Life Technologies	61965059
Critical commercial assays		
NucleoSpin RNA kit	Macherey-Nagel	740955.50
High-Capacity cDNA Reverse Transcription Kit	Applied Biosystems	4368814
GoTaq® Flexi DNA Polymerase kit	Promega	M8291
GeneJET Gel Extraction Kit	Thermo Fisher Scientific	K0691
ExoSAP-IT	Affymetrix	15513687
SsoAdvanced Universal SYBR Green Supermix	BioRad	1725270
2-D Clean-Up kit	GE Healthcare	10298894
jetPrime kit	Polyplus	101000027
Mounting buffer kit for STORM imaging	Abbelight	Smart kit
Duolink *In situ* Red Starter kit mouse/rabbit	Sigma-Aldrich	DUO92101
Experimental models: Cell lines		
HEK293T cells	ATCC	CRL-3216
Oligonucleotides		
See Table S4 for primers sequences		
Recombinant DNA		
IQCH Human Tagged ORF Clone	Amsbio	#RC208441
Software and algorithms		
SeqScape software	Applied Biosystems	4474978
BioEdit software	Ibis Therapeutics	Version 7.2
BioRad CFX Maestro	BioRad	#12004110
ImageJ	Schneider et al., 2012[42]	Version 1.53t
AlphaFold	Jumper et al.[43]	Version v2.2.4
Other		
Superfrost Plus slides	Thermo Scientific Menzel	17234884
Deposited data	European Genome-phenome Archive (EGA).	Study number EGAS00001007423.

RESOURCE AVAILABILITY

Lead contact

Further information and requests for resources and reagents should be directed to and will be fulfilled by the corresponding author, Aminata Touré (aminata.toure@inserm.fr).

Materials availability

Details about the home-made antibody is available upon request to the corresponding author.

Data and code availability

- This paper does not report original code.
- Exome sequencing dataset of the patient is deposited to the European Genome-phenome Archive (EGA) with the study number EGAS00001007423. Any additional information required to reanalyse the data reported in this paper is available from the lead contact upon request.

EXPERIMENTAL MODEL AND STUDY PARTICIPANT DETAILS

Subjects

The study received the approval of the Comité de Protection des Personnes CPP Ile de France III (record number CPP02748) and respects all ethical guidelines (Declaration of Helsinki). An informed consent was obtained from all the subjects prior to their inclusion in the study. The case report (age 46, North African), the four infertile patients with idiopathic asthenozoospermia (age 35 to 46, North Africans and Caucasians) and the five control individuals with normal semen parameters (age 22 to 45, North Africans and Caucasians) were recruited at the Service de Biologie de la Reproductionof the Cochin hospital (Paris).

Human semen samples

Semen samples from the patients and control individuals were obtained by masturbation after 2 to 7 days of sexual abstinence and liquefaction was achieved by incubation at room temperature for 30 minutes. Evaluation of the semen parameters was next performed following the World Health Organization (WHO) updated guidelines.[44] All control individuals displayed normal semen parameters (volume, pH, numeration, motility, viability, morphology) following the WHO criteria.

METHOD DETAILS

Transmission electron microscopy analysis

Sperm cells collected from fresh ejaculate were washed with M2 medium (Sigma-Aldrich Co. Ltd; Irvine, UK) and centrifugated at 300 x g at room temperature for 10 min. Spermatozoa were then fixed fixed in 0.1 M phosphate buffer (pH 7) supplemented with 3% glutaraldehyde (Grade I; Sigma-Aldrich) for 2 h at room temperature. The samples were washed twice in PBS and resuspended in 0.2M sodium cacodylate buffer. The samples were then post-fixed in 1% osmium tetroxide (Electron Microscopy Sciences), dehydrated and embedded in Epon resin (Polysciences Inc.). Semi-thin sections were cut and stained with toluidine blue-Azur II. Ultra-thin sections (90 nm) were cut with a Reichert Ultracut S ultramicrotome (Reichert-Jung AG) and then stained with uranyl acetate and lead citrate prior to observation. A JEOL 1011 electron microscope (Jeol Ltd; Tokyo, Japan) was used to examine the sections and Digital Micrograph software coupled to a Gatan Erlangshen CCD camera allowed the acquisition of images.

Whole exome sequence analysis

Genomic DNA extracted from blood samples was subjected to whole exome sequencing and bioinformatic analyses, as follow. The coding regions and intron/exon boundaries were sequenced on the Novogen platform based in China (agilent v6, HiSeqX,) after enrichment with Agilent kits (Agilent Technologies, Wokingham, UK). All datasets were reanalyzed using our updated bioinformatics pipeline, following the GATK 3.7 best practice recommendations. For this, the sequencing reads were aligned against the GRCh38 reference genome using BWA-MEM 0.7.17 and the resulting BAM files were cleaned and sorted. The duplicates were marked using Picard 2.7.1 and the variants were called using GATK HaplotypeCaller to produce GVCF files. The GVCF files were then merged with a custom script (https://github.com/bcm-uga/mergeGVCFs) to obtain a single GVCF, and a final VCF file was produced with GATK Genotype GVCFs. The candidate variants were identified using an in-house bioinformatics pipeline (Perl scripts available upon request), as follows: Low-quality variant calls (DP<5, GQ<20, or less than 15% of reads supporting the ALT allele) were removed. We used Variant Effect Predictor (VEP version 92) to annotate the variants and predict their impact. All variants with a minor allele frequency greater than 5% in the NHLBI ESP6500 [Exome Variant Server, NHLBI GO Exome Sequencing Project (ESP), Seattle, WA], greater than 3% in 1000 Genomes Project phase 3 datasets, or greater than 1% in gnomAD v2.0 (https://gnomad.broadinstitute.org/) were discarded. We also compared the candidate variants to an in-house database of over 200 control exomes enriched for North African subjects. All variants present in homozygous state in this control database were excluded. We then only retained the variants impacting splice donor or acceptor sites or causing frameshifts, in-frame insertions or deletions, stop gain, stop loss or missense variants except those scored as "tolerated" by SIFT (https://sift.bii.a-star.edu.sg/) and as "benign" by Polyphen-2 (http://genetics.bwh.harvard.edu/pph2/). Gene expression data from the Genotype-Tissue Expression, GTEx project (https://gtexportal.org/home/) were added and used to strengthen the likely implication of the selected candidate variants.

Sanger sequencing

The selected candidate variants were confirmed by Sanger sequencing using ABI 3130XL and SeqScape software (Applied Biosystems; Foster City, CA, USA). The primers for Sanger sequencing are listed in Table S5.

RT-PCR and RT-qPCR analyses

Total RNA was extracted from control and patient spermatozoa (800-1000 ng) using a NucleoSpin RNA kit (Macherey-Nagel; Düren, Germany) and subjected to reverse transcription using a High-Capacity cDNA Reverse Transcription Kit (Applied Biosystems, Thermo Fisher Scientific; Waltham, MA, USA) following the manufacturer's instructions. PCR was performed using a GoTaq® Flexi DNA Polymerase kit (Promega; Madison, WI, USA). Amplicons were purified by exonuclease ExoSAP-IT treatment (Affymetrix, Fisher Scientifix; Pittsburgh, PA, USA) or using a GeneJET Gel Extraction Kit (Fermentas, Thermo Fisher Scientifics; Waltham, MA, USA). Sequencing was performed by Eurofins Scientific (France) and the results were analysed using BioEdit software (Ibis Therapeutics; Carlsbad, CA, USA). cDNA from the patient and control individuals was subjected to RT-qPCR assay using the SsoAdvanced Universal SYBR Green Supermix (BioRad; Hercules, CA, USA). Results were processed using BioRad CFX Maestro and analysed using the ΔΔCt method.[45] Tissue distribution analyses were performed using human MTC panels I & II (636743, Clontech Laboratories; Mountain View, CA, USA). All primers are listed in Table S5.

Immunofluorescence assay

A fresh semen sample was spread on Superfrost Plus slides (Thermo Scientific Menzel) and fixed for 10 min in 4% paraformaldehyde in PBS. Immunostaining was performed as follow. The slides were incubated 20 min at 95 C in citrate buffer (H-3300, VectorLabs) and treated with 0.2% Triton in PBS for permeabilization. After blocking by incubation in 1% BSA for 1 h, the slides were incubated with primary antibodies for 2 h at room temperature. The slides were washed in PBS and then incubated with secondary antibodies for 1 h at room temperature. After washing in PBS, the slides were mounted in Vectashield medium (Vector Laboratories) supplemented with 0.5 mg/mL DAPI. Primary antibodies: rabbit polyclonal anti-IQCH (Sigma HPA040845; "antibody A", 1/100 dilution in PBS/0.02% Triton /1% BSA), home-made rabbit polyclonal anti-IQCH antibody ("antibody B", 1/350 dilution in PBS/0.02% Triton/1% BSA), rabbit polyclonal anti-MAP7D3 (Sigma HPA035598, 1/100 dilution in PBS/0.02% Triton/10% NGS), and mouse monoclonal anti-α-tubulin (Sigma T9026, 1/500 dilution). The specificity of anti-IQCH antibodies A and B was validated by performing transient cell transfection of HEK293 cells with the long isoform of IQCH (IQCH Human Tagged ORF Clone, #RC208441 Amsbio, Abingdon, UK) using the jetPrime kit (Polyplus, Illkirch-Graffenstaden, France). Secondary antibodies: goat polyclonal anti-rabbit IgG Alexa Fluor 568 (Invitrogen A-11029, 1/500 dilution) and goat polyclonal anti-mouse IgG Alexa Fluor 488 (Invitrogen A-28175, 1/500 dilution).

Western-blot analysis

Sperm cells were sequentially washed with M2 medium and then with PBS by centrifugation at 400 x g at room temperature for 10 min. The sperm pellets were then subjected to adapted protein extraction protocols: (I) for IQCH detection with the home-made antibody, the pellets were resuspended and denatured in Laemmli buffer and incubated at 95°C for 5 min, centrifuged at 13,000 x g at 4°C for 10 min, the supernatant collected, and 5% β-mercaptoethanol added prior to incubation at 95°C for 5 min; (II) for IQCH detection with the Sigma HPA040845 antibody, pellets were resuspended and denatured in Laemmli sample buffer with 5% β-mercaptoethanol, homogenized by several passages through a syringe, and incubated at 95°C for 5 min; and (III) for MAP7D3 detection, sperm pellets were resuspended and lysed in 7 M urea, 2 M thiourea, 40 mM Tris, and 4% CHAPS (pH 8.8), supplemented with Complete EDTA-free Protease Inhibitor cocktail (Sigma-Aldrich; St. Louis, MO, USA), and incubated for 1 h on a shaker at 4°C. After centrifugation at 13,800 x g at 4°C for 10 min, the supernatant was purified using a 2-D Clean-Up kit (GE Healthcare; Waukesha, WI, USA). Protein extracts were subjected to SDS-PAGE [8% acrylamide/bisacrylamide (40%, 37.5:1)], transferred to nitrocellulose membranes saturated with PBS/0.1% Tween/5% milk and then incubated with the primary and secondary antibodies at room temperature for 2 h and 45 min, respectively. The primary antibodies were all diluted in PBS/0.1% Tween/5% milk, except the IQCH and MAP7D3 antibodies, which were diluted in PBS/0.1% Tween/3% BSA: rabbit polyclonal anti-IQCH (Sigma HPA040845, called "antibody A", 1/250), home-made rabbit polyclonal anti-IQCH, called "antibody B", 1/500), rabbit polyclonal anti-MAP7D3 (Sigma HPA035598, 1/500), mouse monoclonal anti-β-tubulin clone

AA2 (Sigma 05-661, 1/2500), and rabbit polyclonal anti-GAPDH (CusAb PA00025A0Rb, 1/500). Secondary antibodies were diluted in PBS/0.1% Tween/5% milk: rabbit polyclonal anti-mouse Ig coupled to horseradish peroxidase (HRP) (Dako P0260, 1/1000) and swine polyclonal anti-rabbit Ig coupled to HRP (Dako P0217, 1/1000).

Super-resolution microscopy

Spermatozoa from control individuals were spread and fixed on thick cover slips (22 x 22 mm, 170 ± 5 μm). The staining method was identical to the above immunofluorescence protocol for both the stochastic optical reconstruction microscopy (2D-STORM) and stimulated emission depletion microscopy (STED) techniques. Primary antibodies were diluted in PBS/0.02% Triton/1% BSA: rabbit polyclonal anti-IQCH (Sigma HPA040845, 1/100), mouse monoclonal anti-α-tubulin (Sigma T9026, 1/300), mouse monoclonal anti-calmodulin (Upstate 05-173, 1/100), mouse monoclonal anti-DNAI2 (Abnova H00064446-M01, 1/100), polyclonal mouse anti-DNALI1 (Sigma SAB1406631, 1/100), rabbit polyclonal anti-AKAP4 (Sigma-Aldrich® HPA020046, 1/300), and rabbit polyclonal anti-SLC9C1 (Invitrogen PA5-104160, 1/100). The secondary antibodies for 2D-STORM were goat anti-rabbit Alexa Fluor 555 A-21430 (1/200) and goat anti-mouse Alexa Fluor 647 A-21237 (1/200). The secondary antibodies for STED were goat polyclonal anti-rabbit IgG (Abberior STAR 635P, 1/100) and goat polyclonal anti-mouse IgG (Abberior STAR 580, 1/100). Samples were mounted on adapted microscopic slides with a cavity using the Smart kit (Abbelight, France) or Everspark buffer (Idylle, France) for STORM and in Prolong Gold w/o DAPI buffer (ThermoFisher) for STED. Data acquisition was performed using SR Leica GSD PALM STORM and SR Leica SP8X STED FLIM microscopes.

Proximity ligation assay

The proximity ligation assay was performed using the Duolink *In situ* Red Starter kit mouse/rabbit, DUO92101 (Sigma-Aldrich) following the manufacturer's instructions. In addition to the experiment, a number of experimental controls were performed: (I) a technical negative control without primary antibody; (II) a biological negative control with non-interacting proteins, such as DNAI2 (mouse monoclonal, Abnova H00064446-M01, 1/320 dilution) and SPAG6 (rabbit polyclonal, Sigma HPA038440, 1/200 dilution); (III) a biological positive control with interacting proteins, such as DNAI2 (mouse monoclonal, Abnova H00064446-M01, 1/320) and DNAH17 (rabbit polyclonal Sigma HPA024354, 1/320 dilution); and (IV) the testing condition with IQCH (rabbit polyclonal, Sigma HPA040845 antibody; 1/100 dilution) and calmodulin (mouse monoclonal, Upstate 05-173; 1/100 dilution). Red dots, identifying the proximity between the two targets, were quantified by counting at least 100 spermatozoa per condition and classified into the following three categories: "0 spots", "1 to 3 spots", and "> 3 spots" per spermatozoon.

Structural modelling

Modelling of the interaction complex involving calmodulin and IQCH and mediated by the IQ motif was performed using AlphaFold based on the AlphaFold Colab notebook ([43,46], AlphaFold Colab notebook). Comparisons with published models of calmodulin interaction with IQCG (CaM-IQCG),[25] and Myosin V (CaM-Myosin V)[26] were also performed.

Capacitation assay

The experiment was performed with semen sample from the patient carrying the *IQCH* mutation (Table S1, semen sample II with 60% of sperm viability) together with four asthenozoospermic patients (Table S4) and five control individuals displaying normal semen parameters following the WHO criteria. Fresh ejaculated semen samples were obtained by masturbation after 3–5 days of abstinence. After liquefaction of the semen samples during 30 minutes at room temperature, 2 tubes with 4 x 10^6 spermatozoa were prepared for each individual (t0, t3h) and washed with Ferticult-IVF medium (FertiPro NV, Beernem, Belgium) by centrifugation at 400g during 10 minutes at room temperature. The sperm cell pellets were gently resuspended in 400 μl of Ferticult-IVF medium supplemented with 3% of BSA to reach a final concentration of 10x10^6 cells/ml. For each individual, the 2 tubes were processed as follow: the experimental control tube (t=0) was immediately processed for protein extraction while the reaction tube (t=3h) was incubated for *in vitro* capacitation during 3 hours at 37°C in 5% CO_2. For protein extraction, samples collected at t=0 and t=3 h, were washed with 500μl of cold PBS supplemented with a cocktail of phosphatase inhibitors (PhosSTOP, Roche-Boehringer) by centrifugation at 11000g for 10 minutes. The cell pellets were resuspended in 50 μl of Laemmli buffer and proteins were solubilized by heating at 95°C during 10 minutes. Protein extracts were centrifuged at 11000g for 10 minutes and the supernatants were subjected to SDS–PAGE

by loading 1 x 10^6 cells/lane for each sample. The gels were transferred to nitrocellulose membrane, which was saturated with PBS/0.1% Tween/3% BSA during one hour at room temperature and then incubated with the mouse monoclonal 4G10 antibody (Millipore; dilution 1:1000) at 4°C overnight. After 3 washes in PBS, the membrane was incubated with the rabbit polyclonal anti-mouse Ig coupled to horseradish peroxidase (HRP) (Dako P0260, 1/1000) during 45 minutes at room temperature and then washed in PBS and processed for signal detection by chemiluminescence (WesternBright ECL Spray- Advansta, VWR, France). The membrane was next probed with mouse monoclonal anti-β-tubulin clone AA2 (Sigma 05-661, 1/2500) following the same experimental procedure.

QUANTIFICATION AND STATISTICAL ANALYSIS

Super resolution microscopy data analysis

STORM images were processed using the ThunderStorm ImageJ plugin. Signal intensity RGB profiles were acquired from transversal sections of at least four sperm flagella per experimental condition. The protein distribution was evaluated by measuring the peak width and the distance from the central axis.